Title

Size-Dependent Nascent Sea Spray Aerosol Bounce Fractions and Estimated Viscosity: The Role of Divalent Cation Enrichment, Surface Tension, and the Kelvin Effect.

Journal

Environmental Science & Technology, 58(44)

Authors

Tumminello, Paul

Niles, Renee

Valdez, Vanessa

et al.

Publication Date

2024-11-05

DOI

10.1021/acs.est.4c04312

Peer reviewed

Environmental Science & Technology

pubs.acs.org/est

Article

Size-Dependent Nascent Sea Spray Aerosol Bounce Fractions and Estimated Viscosity: The Role of Divalent Cation Enrichment, Surface Tension, and the Kelvin Effect

Paul R. Tumminello, Renee Niles, Vanessa Valdez, Chamika K. Madawala, Dilini K. Gamage, Ke'La A. Kimble, Raymond J. Leibensperger, III, Chunxu Huang, Chathuri Kaluarachchi, Julie Dinasquet, Francesca Malfatti, Christopher Lee, Grant B. Deane, M. Dale Stokes, Elizabeth Stone, Alexei Tivanski, Kimberly A. Prather, Brandon E. Boor, and Jonathan H. Slade*

Cite This: *Environ. Sci. Technol.* 2024, 58, 19666−19678

Read Online

ACCESS | Metrics & More | Article Recommendations | Supporting Information

ABSTRACT: Viscosity, or the "thickness," of aerosols plays a key role in atmospheric processes like ice formation, water absorption, and heterogeneous kinetics. However, the viscosity of sea spray aerosols (SSA) has not been widely studied. This research explored the relationship between particle size and viscosity of authentic SSA particles through particle bounce, atomic force microscopy analysis, and predictive viscosity modeling from molecular composition. The study found that 40 nm SSA particles had estimated viscosities around 10^4 Pa·s and bounce fractions three times higher than 100 and 200 nm particles with less than 10^2 Pa·s at a relative humidity (RH) of 60%. Additional studies revealed the Kelvin effect and particle density, influenced by particle size, have a greater impact on size-dependent bounce fractions than changes in RH across impactor stages. While changes in the level of surfactants can impact particle bounce, the increased viscosity in smaller SSA is attributed to the formation of gel-like phase states caused by cation−organic cross-links between divalent calcium ions and organic anions enriched in the smaller particles. This work shows the smallest gel-like SSA particles observed in the field are highly viscous, which has implications for cloud formation, secondary aerosol growth, and pollutant transport in coastal environments.

KEYWORDS: *SSA, gels, phase, viscosity, bounce, ELPI*

1. INTRODUCTION

Sea spray aerosol (SSA), generated through wave breaking, constitutes a significant portion of the global aerosol mass load.[1] SSA is a complex mixture of inorganic salts, organic carbon (OC), and biological material, which varies with seawater biological activity and particle size.[2−11] The composition and chemical mixing state of SSA impact visibility, ice, cloud, fog formation, and air quality in marine environments.[6,7,12−15]

Aerosols adopt various phase states, or viscosities, depending on properties such as their density,[16,17] surface tension,[11,18−20] chemical composition (i.e., molecular weight,[21−24] oxygen-to-carbon ratios (O/C),[25−27] organic to inorganic ratios[23,28−30]), and external environmental conditions such as relative humidity (RH)[31−33] and temperature.[21,24,34,35] The particle phase affects depositional ice nucleation,[36,37] water uptake and cloud condensation nucleus activity,[8,38−40] and heterogeneous reactivity.[32,41]

Single-particle atomic force microscopy (AFM) has shown that more viscous or solid-like phase states exist in nascent (i.e., freshly emitted) submicron SSA particles in samples collected from a controlled wave flume in the presence of a phytoplankton bloom.[11] These more viscous states were associated with a larger volume fraction of OC and more core−shell-type particles. Another showed that nascent SSA particles bounced/rebounded off a rigid surface at a higher fraction, indicating the presence of more viscous nascent SSA phase states during peak phytoplankton activity.[42] Using a mixed aqueous electrolyte/OC/water aerosol viscosity model, the bouncier particles were attributed to a greater fraction of higher molecular weight and less hygroscopic OC components.[42]

Received: May 8, 2024
Revised: October 8, 2024
Accepted: October 14, 2024
Published: October 23, 2024

The composition of nascent SSA depends on particle size.[2,39] A study by Ault et al., 2013[39] showed the presence of two distinct submicron nascent SSA populations—larger-sized particles composed of NaCl cores coated in OC mixed with cations such as Mg^{2+}, and smaller-sized homogeneously mixed particles composed of OC combined with cations and anions. Macromolecules, including lipopolysaccharides (LPS), can interact electrostatically in polyelectrolytes, forming colloidal organic material, marine gels, and transparent exopolymer particles (TEP) of varying sizes.[43] Although emphasis has been on their formation in surface water,[43−45] marine colloids, gels, and TEP are also found in SSA.[46−49] Some studies have found that TEP is more enriched with decreasing SSA size.[46,47] Salter et al. 2016[50] also showed SSA particles collected over the North Atlantic region were increasingly enriched (relative to Na^+) in divalent Ca^{2+} with decreasing particle size, with approximately 50% of the total inorganic ion mass and greatest enrichment in 0.029−0.06 μm SSA from Ca^{2+}, followed by K^+, Mg^{2+}, SO_4^{2-}, and Cl^-.[50] These divalent cations are especially important in promoting the transfer of LPS in SSA[4] through cross-linking. The cation−organic cross-links form gel-like phase states.[49,51] The expected more viscous gel-like phase states have important implications for particle water uptake and reactivity. Previous research showed water uptake in SSA-like mimics depended on the type of fatty acid and the identity of the halide ion.[52,53] Furthermore, Lee et al., 2021[54] showed that divalent cation-driven LPS morphological changes kinetically hindered heterogeneous reactions between gas-phase HNO_3 and SSA. Through the enrichment of cross-linking divalent cations in smaller SSA particles, it is expected that phase state will also vary with particle size. However, this has not been demonstrated systematically for nascent SSA.

Lee et al. 2020[55] and Kaluarachchi et al. 2022[56] first measured the size-resolved phase states and morphologies of nascent SSA particles collected via impaction onto Micro-Orifice uniform deposition impactor (MOUDI) stages. They reported a trend toward more liquid-like particles with increasing particle diameters greater than 100 nm. To our knowledge, the phase states of nascent SSA particles with diameters smaller than 100 nm have yet to be studied. Although particles in the ultrafine size range contribute less to the total SSA mass, they can dominate SSA number concentrations and significantly impact the microphysical and radiative properties of clouds.[57]

In this study, we determined the particle bounce fractions and estimated viscosities of nascent SSA generated in a wave flume mesocosm in the presence of wind. We did this as a function of particle size, contrasting the Aitken mode (40 nm) with the accumulation mode (200 nm). Size-dependent nascent SSA phase states and morphologies of single particles using AFM are also presented. The size-resolved nascent SSA particle viscosities were estimated from average bulk aerosol chemical properties, including O/C, molecular weight, OC and inorganic mass fractions, and effective densities using a mixed organic/aqueous electrolyte aerosol viscosity model.[42,58−62] Independent of the chemical composition, the effects of density, surface curvature, surface tension, and RH drops in the impactor on the size-resolved particle bounce fractions are described. This work highlights the importance of particle size on nascent SSA phase states, which are crucial for understanding their atmospheric processing, cloud-forming potential, and reactivity.

2. EXPERIMENTAL METHODS

2.1. CHAOS Experimental Description. This work was conducted at the Scripps Institution of Oceanography (SIO, La Jolla, CA) utilizing the Scripps Ocean Atmosphere Research Simulator (SOARS) during the 2022 laboratory-intensive characterizing atmospheric-oceanic parameters of SOARS (CHAOS) campaign as part of a large collaborative study by scientists in the National Science Foundation Center for Aerosol Impacts on Chemistry of the Environment (NSF-CAICE).[63] The SOARS wave flume was filled with seawater during a period of low biological activity [i.e., chlorophyll-*a* (chl-*a*) concentrations <0.2 μg L^{-1}] collected at the Scripps Pier (La Jolla, CA; 32° 51′ 56.8″ N; 117° 15′ 38.48″ W), prefiltered using sand trap filters and a 1 μm mesh filter to remove bacterial grazers. Nascent SSA inside the wave flume was generated by an air-backed paddle that generated breaking waves in the middle of the channel, terminating on an artificial beach to prevent reflective wave-breaking action. Using two small fans, the wave flume headspace maintained slight positive pressure to prevent room air contamination. Between changing wind speeds, aerosol particle concentrations were measured simultaneously inside the wave flume without SSA generation (i.e., no waves) and in the surrounding room air. The headspace was recirculated through HEPA and Carbon Clean 16 filters to scrub the remaining SSA and particulates, while a freshwater sparging system cleaned the headspace of SSA accumulation. This approach removed more than 95% of the particles compared to room air.[64] The example aerosol size distributions in Figure S1 show significantly fewer aerosols in the wave flume after filtering than ambient air outside the wave flume at all measured sizes in the submicron range. Typical room air concentrations were a few thousand particles cm^{-3} compared to ~10^4 cm^{-3} in the SOARS headspace with winds and waves and ~10^2 cm^{-3} in the SOARS headspace while filtering with winds. Wind was generated in the recirculatory headspace of SOARS to simulate winds over the open ocean using a dual fan setup with a 10 m extrapolated wind speed of ~19 m s^{-1} (wind speeds were measured at 0.6 m height in SOARS and extrapolated to a 10 m height value using Gilhousen et al.).[65] At these wind speeds, film, jet, and spume drops are expected to contribute to SSA production.[66] The wave state at a wind speed of 19 m/s within SOARS was described by Madawala et al., 2024.[64] Because the wave amplitude was fixed, the whitecap coverage within SOARS cannot be compared directly to the open ocean. However, the average whitecap coverage in Monahan and O'Muircheartaigh[66] was used to calculate the wave field generated by the paddle, showing similar coverage to that of an open-ocean wave field in equilibrium with a wind speed of 18.5 m/s.[66] Headspace air was recycled within the flume to minimize outside contamination and concentrate the SSA particle load. The headspace's temperature (T) and RH were monitored during the operation of SOARS and nominally at ~25 °C and ~85−90%, respectively.

2.2. SSA Sampling Apparatus. A diagram of the aerosol sampling setup can be found in Figure S2. Briefly, SSA was sampled from the headspace at~3/4 of the length of SOARS following an equilibration time of 20 min for the nascent SSA size distributions to reach a steady state in the SOARS headspace. The particles, which exited the headspace up to 95% RH at a flow rate of 1LPM, were equilibrated to ~55 (±5)% RH (nonefflorescing) through a silica diffusion drier

https://doi.org/10.1021/acs.est.4c04312
Environ. Sci. Technol. 2024, 58, 19666−19678

before passing through a differential mobility analyzer (DMA) (BMI 2100, Brechtel Inc.) for size selection (electrical mobility classification). Aerosol particles were size selected by their electrical mobility diameters across four distinct size bins (40, 60, 100, and 200 nm), with the average and max and min size distributions during the study in Figure S3. The reason for the large spread in the number concentration in Figure S3 (shaded regions) is not entirely apparent. However, at the relatively high wind speeds, we've noticed less stability in SSA number concentrations compared to lower wind speeds, which we hypothesize may be driven by secondary aerosol production, e.g., from the secondary aerosolization from impaction of spume droplets that have not achieved equilibrium in the headspace. This would influence the total particle numbers, but it is unclear if the specific mechanism generating the SSA influences its physical properties with respect to the sizes examined in this study, requiring additional analysis beyond the scope of this study. The reported diameters were considered wet or nonefflorescsed, which, according to the SSA growth factors reported in Bertram et al. 2018,[6] would equate to dry sizes of 17, 26, 43, and 87 nm at 0% RH, respectively. The SSA size distribution in Figure S3 exhibits a significant fraction of nucleation and Aitken mode particles. This is comparable to the ambient open ocean measurements by Schwier et al., 2015[67] and Ovadnevaite et al., 2014,[68] and different from Prather et al., 2013,[2] where SSA was generated without winds. Given the low background aerosol concentrations within SOARS (i.e., <5% of ambient), as shown in Figure S1, the higher SSA concentrations in this size range than in Prather et al., 2013[2] cannot be attributed to contamination. As described by Ovadnevaite et al., 2014[68], the higher concentration of nucleation and Aitken mode SSA particles in this study could be attributed to higher wind speeds, leading to larger Reynolds numbers. Their study found a greater SSA production flux in these size ranges at higher wind speeds than in slower or no wind conditions. Additionally, Schwier et al., 2015[67] suggested that the presence of organic material at the surface is associated with the production of particles in the nucleation and Aitken size modes. The monodisperse aerosol stream was further diluted with ∼19 LPM of HEPA-filtered room air while sampling with two electrical low-pressure impactors (ELPI+; Dekati Ltd.) that sampled simultaneously at a combined flow rate of 20 LPM. Utilizing two ELPIs in tandem enabled real-time determination of SSA phase state and effective densities.[69] The RH and T of the sample flow at the inlet of the two ELPIs were monitored with an in-line sensor (Vaisala) and were stable at a RH of ∼55 (±5)% and T of ∼27 (±2) °C, the same as the conditions before size selection. This indicates that particle size and phase state were unchanged during electrical mobility classification.

2.3. Particle Bounce Analysis. A description of the ELPI, its operation, and measurements of particle bounce fractions are detailed in previous studies.[42,60,62] Briefly, aerosols were unipolarly charged at the inlet from a corona charger, and the charged particles were detected with sensitive electrometers based on their current (I) during collection across a 15-stage electrically insulated cascade impactor. The relationship between I and particle number concentration, N, is defined as follows

$$I = PneUN \tag{1}$$

where P is the penetration efficiency of particles through the ELPI inlet, n is the average number of charges on the particle, e is the elementary charge, and U is the volumetric flow rate.

This study used two ELPIs simultaneously, one prepared with smooth Al-foil substrates that allowed particle bounce and the other with sintered collection substrates coated with a thin film of vacuum grease that inhibited particle bounce.[60,62,70−73] Exemplary size distributions and comparisons between the integrated currents of both ELPIs are shown in Figure S4 and described in the Supporting Information. The Nascent SSA bounce factors (BF) were calculated as defined in eq 2, where I_{1+2}^{foil} and $I_{1+2}^{\text{sintered}}$ represent the summed current from the impactor filter stage (1) and the stage immediately preceding it (2) for the Al-foil and sintered ELPI plates, respectively. Including both bottom stages ensures that most of the current resulting from bounced particles was accounted for, as some bounced particles stopped bouncing in stage 2. I^{sintered} refers to the sintered ELPI current, and the denominator represents the sum of the sintered ELPI currents from stages 3 to 14.[42] The currents were corrected for the presence of multiply charged particles before calculating BF.[69]

$$\text{BF} = \frac{I_{1+2}^{\text{foil}} - I_{1+2}^{\text{sintered}}}{\sum_{n=3}^{14} I^{\text{sintered}}} \tag{2}$$

Currents were allowed to stabilize for 5 min before data collection at a sampling rate of 1 Hz for each of the four size-selected electrical mobility diameters (40, 60, 100, and 200 nm). Due to some noise in the currents measured at 1 Hz, the BF values reported herein were determined from 30 s averaged currents.

2.4. Single Particle Morphology and Phase State Analysis with AFM. Freshly emitted SSA particles were deposited onto silicon substrates (coated with hydrophobic Rain-X) at ∼50% RH, using a MOUDI (MSP, Inc., model 125R) at a flow rate of 10 LPM. The SSA samples (volume−equivalent diameter range of 0.04−0.2 μm) collected during the wind speed condition at ∼10 m height above the water level in SOARS (19 m/s) were selected to investigate the physicochemical properties (i.e., morphology and phase state) of individual SSA particles for comparison with the BF measurements. Volume equivalent diameters, commonly reported in AFM studies,[11,55,74−78] refer to the diameters of a sphere of the same volume as the particles measured with the AFM, which can differ from aerodynamic diameter (measured by the ELPI) or electrical mobility diameter (measured by the DMA) depending on the particle's shape, density, or electrical charge. Reported diameters are specified according to how they were measured and left as is. The relative distribution of main morphologies (rounded and core−shell) and phase states in two volume-equivalent size ranges, 0.04−0.1 μm and 0.1−0.2 μm were compared.

A molecular force probe 3D AFM (Asylum Research, Santa Barbara, CA) was used to image individual SSA at ∼20% RH and ambient temperature (20−25 °C) and pressure as described in prior studies.[55,77,78] A custom-made humidity cell was used to control RH to 60%. Prior to the AFM measurements at a particular RH, a waiting time of at least 10 min was allocated to ensure the substrate-deposited SSA was in thermodynamic equilibrium with surrounding water vapor at the corresponding RH.[7,11,76] Silicon nitride AFM tips (MikroMasch, model CSC37, tip radius of curvature ∼10 nm, nominal spring constant 0.5−0.9 N/m) were used for

https://doi.org/10.1021/acs.est.4c04312
Environ. Sci. Technol. 2024, 58, 19666−19678

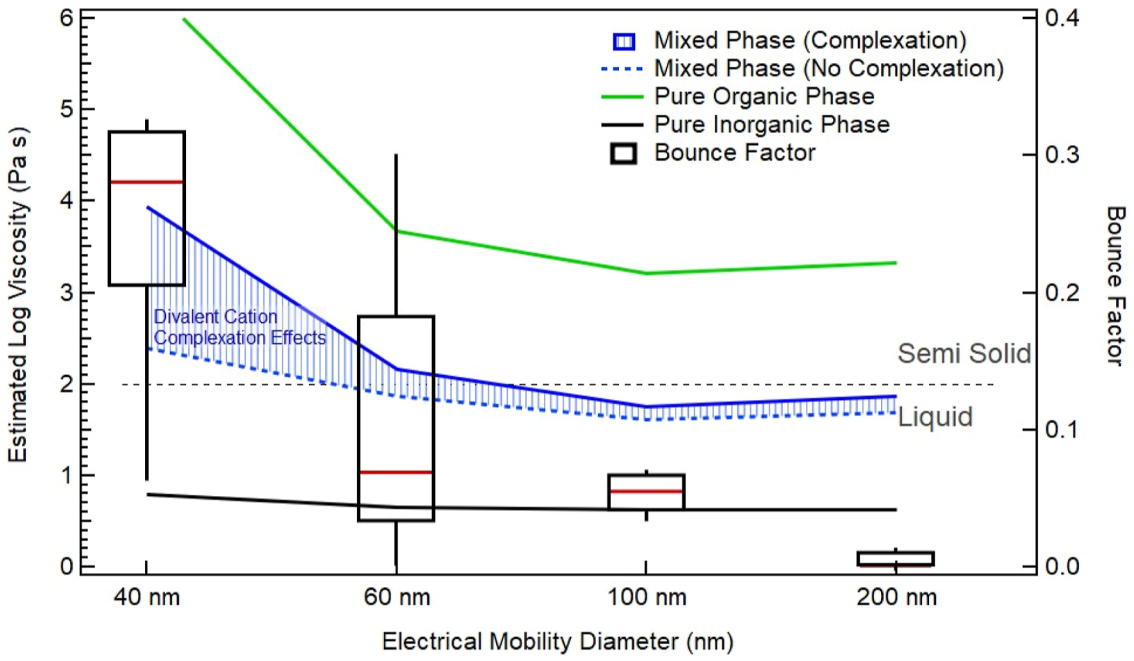

Figure 1. BF box and whisker plot representing the median (red line), 25th and 75th quartiles (boxes), and maxima and minima (whiskers) for size-selected nascent SSA during CHAOS. Modeled viscosity of nascent SSA assuming an OC/aqueous electrolyte aerosol mixture at an RH of 50%. Shaded region refers to a range of modeled viscosity due to molecular weight increases resulting from divalent cation complexation. The black and green curves indicate the viscosities for the inorganic-rich and organic-rich phases of the nascent SSA, respectively.

AFM imaging and force spectroscopy measurements.[76,79] As described previously, the AFM AC (intermittent contact) imaging mode was used to collect 3D height images of individual SSA to determine their morphology and quantify their volume−equivalent diameter.[56,78] For morphological analysis, approximately 40 individual particles were studied for each sample type, and the relative abundance (i.e., average with one standard deviation for a fraction of particles) of identified main morphological categories (rounded, core−shell, prism-like, rod, and aggregate) were examined within the size range of 0.04−0.2 μm.

Since the total number of individual particles that can be realistically studied with the AFM approach is somewhat limited, a statistical analysis was employed to assess the statistical significance of the AFM measurements. A detailed description of the approach can be found elsewhere.[56,80] Based on the analysis, an average with one standard deviation for the fraction of particles from each morphological type or one of three phase states (solid, semisolid, and liquid) was determined.

The phase state identification at 60% RH was conducted as described previously.[7,55] Briefly, AFM (i.e., force plots), under ambient temperature (20−25 °C) and pressure, was performed on individual particles at a particular RH by probing at the shell region of core−shell and approximately at the center of rounded particles. The maximum force of 20 nN and scan rate of 1 Hz were used, and at least five repeated force plots were collected for each particle at a particular RH. The collected force plots were then used to quantify the viscoelastic response distance (VRD, nm), which can be related to the viscoelastic nature of a solid (higher VRD values generally correspond to lower viscosity), and the relative indentation depth (RID, ratio of the indentation depth over the particle height) for an individual particle at a particular RH.[55,58] A previously reported framework based on the VRD and RID measurements was then utilized to identify each particle's phase state at 60% RH.[7] Approximately 6−10 individual SSA particles of each morphology type were investigated for the phase state identification.

2.5. Organic and Sea Salt Mass Fraction via Thermal Optical Analysis and High-Performance Ion Exchange Chromatography with Conductivity Detection. SSA particles were collected for offline chemical analysis using a high-flow impactor (TSI model 129). Samples were collected at a flow rate of 100 LPM within a RH range of 81−86%. The impactor had three impaction stages with 50% cutoff aerodynamic diameters of 25 μm (prefilter), 1 μm, and 0.25 μm. Particles collected in stages below 0.25 μm did not generate sufficient mass for analysis. A 75 mm quartz fiber filter was used for the prefilter, while 75 mm Al foil substrates were used for the middle impaction stages. These impaction stages were followed by a 90 mm quartz fiber after filter (<0.25 μm). All substrates were baked at 500 °C for 18 h before sample collection. After collection, samples were stored in prebaked aluminum foil-lined Petri dishes at −20 °C.

A thermal optical analyzer (Sunset Laboratories, Forest Grove, OR) measured OC.[81] OC was defined as C evolved from the filter before introducing oxygen. EC was not detected. Organic matter (OM) was estimated by multiplying OC by 1.6 to account for water-soluble and water-insoluble OM mass.[6,48]

Inorganic ions were extracted using water-soluble extraction as described in Shafer et al. 2010[82] and were measured via high-performance ion exchange chromatography with conductivity detection on a Dionex Aquionics DX-1000. Anions were measured using a Dionex AS4A-SC/AG4A-SC column set and ADRS 600 anion suppressor, while cations were measured using a Dionex CS12A/CG12A column set and CSRS 200 cation suppressor. Sea salt was estimated by converting the measured sodium mass to sea salt mass using the ratio of 3.26.[83]

https://doi.org/10.1021/acs.est.4c04312
Environ. Sci. Technol. 2024, 58, 19666−19678

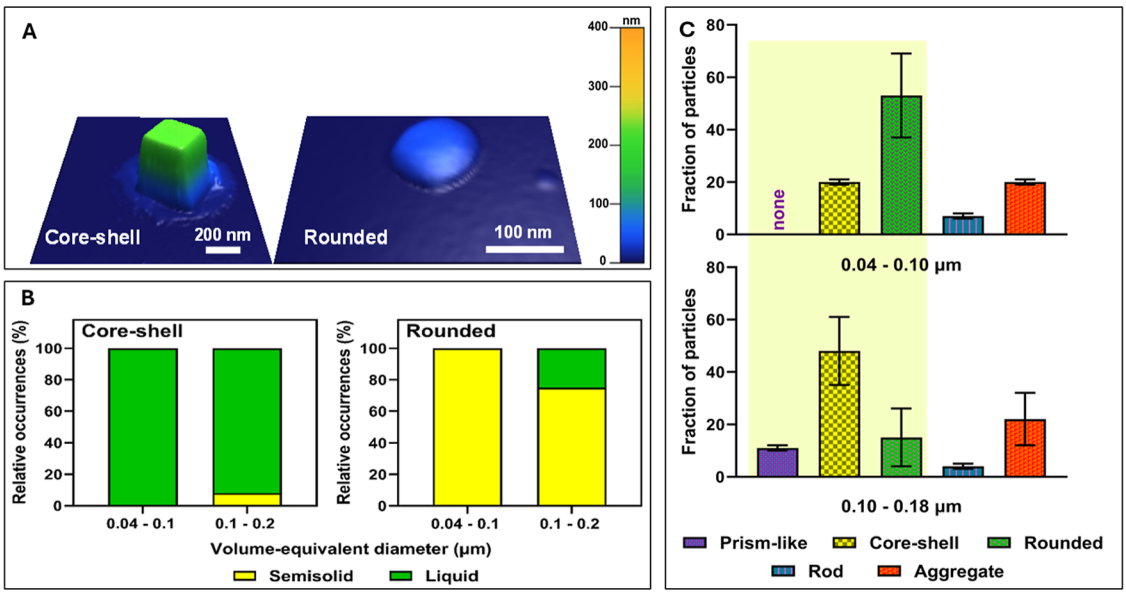

Figure 2. (A) Selected representative AFM 3D-height images at 20% RH of two main SSA morphological categories (core−shell and rounded). (B) Relative distributions of semisolid and liquid phase states at 60% RH for shell regions of core−shell particles and rounded SSA at two volume-equivalent diameter ranges of 0.04−0.1 and 0.1−0.2 μm at 19 m/s wind speed condition. Note that no solid particles were observed. (C) Average and one standard deviation of the fraction of particles (%) from five main morphological categories at two selected volume−equivalent diameter ranges of 0.04−0.1 and 0.1−0.2 μm at 19 m/s wind speed condition.

3. RESULTS AND DISCUSSION

3.1. Nascent SSA Phase State and Dependence on Particle Size. The BF data for size-selected SSA particles during CHAOS are presented in Figure 1, with time-resolved BF data shown in Figure S5, and detailed statistics for each median distribution are available in Table S1. These measurements occurred on different days throughout the study, and not all sizes were sampled on the same day, as shown in Figure S5. However, the SSA was generated from the same ocean water sample under relatively low phytoplankton abundance ([chl-a] < 0.2 μg L^{-1}) and at the same wind speed on all sampling days. While the particle composition is not expected to differ significantly between measurement days under these conditions, it is noted that variations in the organic mass fraction could cause differences in the BF, as shown for secondary organic aerosol particles when mixed with different amounts of inorganic sulfate.[60,84] This point is highlighted further in the modeling results in Figure S9 that show a strong dependence of viscosity on the aerosol organic mass fraction. The presence of surfactants and differences in the fractionation of inorganic ions in the particles, hygroscopicity of the organic components, and molecular weight may also affect particle viscosity and bounce, as shown in Figures S6−S10, and thus, may cause some of the variability in the BF across different measurement days. Days of overlap in the BF between 40 and 200 nm occurred on 8/9, 8/10, and 8/13, and between 40, 100, and 200 nm on 8/13 (Figure S5). There were 2 days of overlap (8/17 and 8/18) between 60 and 200 nm, and 1 day of overlap on 8/17 between 60, 100, and 200 nm.

To put these results in context, previous research on biogenic SOA suggested a BF of ≤0.2 represents liquids, 0.2 ≤ BF ≤ 0.8 are semisolids (or mixture of liquids and solids), and those with a BF of ≥0.8 are solids or glasses.[33] In our previous study, during similar periods of low chl-a abundance as in this study, polydisperse nascent SSA exhibited a BF of ∼0.2, resembling liquids from viscosity estimates.[42] In the same study, a BF of ∼0.8, resembling semisolids, was observed during a high biological activity period ([chl-a] > 10 μg L^{-1}).

The particles selected based on an electrical mobility diameter (d_m) of 40 nm exhibited a median BF (red line) of approximately 0.29, indicating that around 29% of the 40 nm particles bounced upon sampling. 70% of the SSA particles sampled at 40 nm (the difference between the 95th and 25th percentiles) in repeated measurements on different days exhibited a BF akin to semisolid SOA particles (i.e., BF > 0.2). In contrast, up to 25% of the SSA population (25th percentile) sampled at 40 nm over repeated measurements on different days (Figure S5) adopted a BF resembling that of liquid SOA particles (i.e., BF ≤ 0.2), occurring on 8/11.

SSA particles with d_m = 60 nm had a median BF of approximately 0.06, roughly four times less than the 40 nm SSA particles, driven by the measured low BF at this size on 8/16 and 8/17. In this case, the 75th percentiles indicate a BF of <0.2 (indicative of liquid-like particles), while only approximately 15% of the SSA population at this size, sampled over repeated measurements, displayed a BF of >0.2, occurring on 8/18. As larger SSA particles were sampled, BF decreased, with a median BF of ∼0.05 for d_m = 100 nm (8/13 and 8/17 in Figure S5) and ∼0 for d_m = 200 nm (8/9, 8/10, 8/13, 8/17, and 8/18 in Figure S5). Larger SSA particles in these size ranges also demonstrated less variability in BF, as evidenced by the narrow gap between the 25th and 75th percentiles, suggesting a more uniform population of mostly liquid-like SSA particles in this size range. This analysis highlights a pronounced size dependence on the SSA phase state, with larger particles increasingly exhibiting a liquid-like character.

Single particle analysis of the morphology and phase states of the nascent SSA was conducted using AFM to compare with bounce measurements. Individual SSA particles were categorized into two distinct size ranges: 40−100 nm and 100−200 nm in volume equivalent diameter. The rounded morphology (depicted in Figure 2A) was predominately observed for

https://doi.org/10.1021/acs.est.4c04312
Environ. Sci. Technol. 2024, 58, 19666−19678

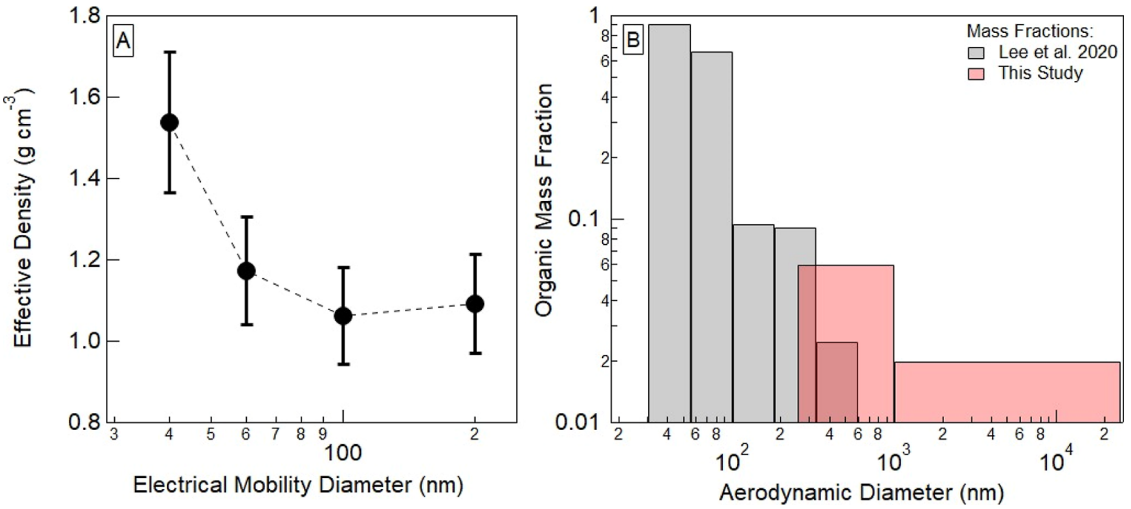

Figure 3. (A) Calculated effective densities for each size selected population and (B) size-resolved organic mass fractions (OMF) obtained for sub- and supermicron nascent SSA populations during this study (red) compared to size-resolved OMF reported in Lee et al. 2020[55] obtained during the peak of an induced phytoplankton bloom.

particles in the 40−100 nm size range (as shown in Figure 2C), while the core−shell morphology (also shown in Figure 2A) was more prevalent in particles sized 100−200 nm (as illustrated in Figure 2C). As depicted in Figure 2B, morphologically dependent phase state analysis revealed that the shells of core−shell particles in both size ranges at 60% RH were predominately liquid, while rounded SSA was mostly semisolid. Considering the higher occurrence of rounded particles in the smaller size range, a primarily semisolid phase state of the nascent SSA would be anticipated, consistent with the observations from size-selected bounce factor analysis of the bulk aerosol population. As the particle diameter increased to 100−200 nm, this analysis indicates a shift toward a greater prevalence of liquid-like core−shell particles, mirroring the trends observed in BF with increasing size.

It is important to note that the core−shell morphology particle shown in Figure 2A, derived from offline AFM analysis, may not represent the particle's morphology during the online bounce measurements. Collected particles for offline AFM analysis were dried to 0% RH in the cell, below the efflorescence RH of sea salt, then rehumidified to 60% RH, below the deliquescence RH. The bounce measurements were performed at ∼55% RH, and therefore did not experience the same RH gradient as the particles within the AFM cell. Therefore, only the phase states of the liquid-like organic shell of core−shell particles (blue region of the particle in Figure 2A), expected to equilibrate to the ambient RH, were compared with rounded morphology particles.

Furthermore, these findings align with the work of Kaluarachchi et al., demonstrating that individual SSA particles with volume equivalent diameters ranging from 100 to 600 nm became more semisolid as their diameter decreased at the peak of an induced phytoplankton bloom.[56] Our analysis extends this understanding, indicating that SSA particles exhibit increased viscosity even at smaller sizes, down to 40 nm without a phytoplankton bloom. Several factors could influence the observed trend in BF with particle size, including size-dependent changes in the particle composition,[2,39,85] morphology,[11,56] and liquid water content.[21,22,30,86,87] In the following sections, we examine the different factors influencing this trend.

3.2. Role of Density and OC across Different Sizes.

Particle density (ρ) plays a critical role in governing the kinetic interactions during an aerosol's rebound from a rigid surface.[88,89] Due to their greater mass, particles with larger ρ but equal volume possess relatively greater kinetic energy upon impact.[24,88] If this additional kinetic energy for particles with higher ρ is preserved, particles with greater density are expected to exhibit higher rebound energy and bounce more, provided that the outgoing rebound potential energy exceeds the energy lost to particle deformation and surface adhesion interactions.[59−62] To evaluate this, we calculated the effective density (ρ_e) using the relationship between electrical mobility and aerodynamic diameters outlined in the Supporting Information. Importantly, Rostedt et al., 2009 demonstrated good agreement between bulk ρ and aerosol ρ_e for both organic and inorganic aerosol compounds.[90]

As shown in Figure 3, ρ_e (circles) showed a decreasing trend with increasing particle diameter, ranging from approximately 1.5 g cm^{-3} for particles with d_m = 40 nm to around 1.0 g cm^{-3} for particles with d_m = 200 nm, reflecting the trend observed in BF with increasing particle size. Since the ELPI size cutoffs are based on aerodynamic diameter, assuming a particle density of 1.0 g cm^{-3}, a calculated ρ_e > 1.0 g cm^{-3} indicates a deviation between the measured aerodynamic diameter and the initially size-selected d_m.

The ρ_e of the 40 nm nascent SSA are comparable to those typical of OC-based aerosols or mixtures with higher density salts (1.5 g cm^{-3}),[91,92] whereas the ρ_e of 100 and 200 nm nascent SSA were lower (∼1.0 g cm^{-3}). This shift may be attributed to an increasing presence of hygroscopic NaCl with increasing size (i.e., less OC), consequently increasing the liquid water mass fraction in larger SSA particles.[2,56] The OC and inorganic salt content in SSA have important impacts on its density, and is expected to vary depending on the particle's size, wind speed, and biological activity. Greater OC content is expected to transfer into smaller SSA particles in regions with high biological activity and low wind speed.[93] This may lead to the smallest particles exhibiting a density more like the OC in the particles. The sea surface layer can be disrupted at higher wind speeds, leading to lower OMF in SSA.[93] This may lead to the particles developing a density more like the inorganic salt

https://doi.org/10.1021/acs.est.4c04312
Environ. Sci. Technol. 2024, 58, 19666−19678

transferred into the particles. As discussed in Salter et al., 2016[50], the fractionation of inorganic salts in SSA differs with particle size. Average values of supermicron (1−25 μm) and submicron (0.25−1 μm) SSA OMF collected during CHAOS are depicted in Figure 3B (red bars). The average and standard deviation in OMF was 0.02 ± 0.01 for 1−25 μm SSA and 0.06 ± 0.03 for 0.25−1 μm SSA based on an analysis of three collection days (8/15, 8/16, and 8/17), indicating that OMF increased with decreasing particle size. Differences in OMF between days are in the Supporting Information (Table S2). Although there were no compositional measurements in a size range comparable to our BF measurements, we can reasonably approximate from the OMF reported by Lee et al., 2020 (as depicted in Figure 3B in gray)[55] that the OMF continued to increase in particles smaller than 0.25 μm in diameter. Despite the good agreement in OMF between this study and Lee et al., 2020[55] in the size range between 0.25 and 1 μm, it is worth noting that the SSA OMFs determined by Lee et al., 2020[55] were collected during the peak of an induced phytoplankton bloom ([chl-*a*] ∼ 5 μg L^{-1}) in the absence of winds. In contrast, this study collected particles without an induced phytoplankton bloom ([chl-*a*] < 0.2 μg L^{-1}) in the presence of winds and a wind speed of U_{10} = 18.9 m s^{-1}. Although parametrizations exist for SSA OMF as a function of particle size, wind speed, and [chl-*a*], they are based on SSA composition measurements over biologically active North Atlantic regions.[48,93] How well this parametrization represents the SSA produced from SOARS with relatively low [chl-*a*] in the seawater remains unclear. However, under the experimental conditions here, the parametrization in Gantt et al., 2011[93] yields an OMF estimate of <0.05 for 40 nm SSA, which is significantly less than expected given the agreement between the measured OMF in this study and that from Lee et al., 2020[55] in overlapping size ranges. The reason for this discrepancy is not fully understood, but it is noteworthy that in addition to chl-*a*, seawater particulate OC (SW-POC) and colored dissolved and detrital organic material (CDM) affect the OMF in SSA, and the apparent lag time between their concentrations in seawater and when organic components become transferrable in SSA also means that the OM in SSA is not necessarily in phase with the organic components in seawater.[94]

3.3. Estimated Size-Dependent Viscosities of Nascent SSA from Bulk Molecular Properties and the Role of Divalent Cation Enrichment and Potential Gel Formation. Figure 1 shows the modeled viscosities for each size-selected nascent SSA population in three phases: a well-mixed homogeneous OC/aqueous electrolyte particle phase (blue), a purely OC phase (green), and a purely aqueous electrolyte phase (black). The aqueous electrolyte particle phase in the model was predicted from a mixture of H_2O, NaCl, and $CaCO_3$. Their proportions within the particle phase and relative to the OC-rich phase were allowed to vary with particle size in the model, with more details on this and the viscosity calculations provided in the Supporting Information. Our viscosity calculations for SSA indicate that increasing particle size leads to a 100× greater predicted liquid water volume due to the higher fraction of hygroscopic inorganic salt in the largest particles.

For the mixed phase, we predicted a $\log_{10}\eta$ (Pa s) of ∼4 for the 40 nm SSA, suggesting semisolid characteristics[21] and resembling that of other organic aerosols, such as simple saccharides like sucrose and levoglucosan.[95,96] The viscosity decreased for larger particles, with $\log_{10}\eta$ (Pa s) decreasing to around 1.8 for the 100 and 200 nm SSA particles. This estimated viscosity closely aligns with our previous prediction of nascent SSA viscosity during a period of low biological activity,[42] as well as the reported viscosity for a 1:2 NaCl and sucrose mixture.[95]

This reduction in estimated viscosity may stem from a decrease in less hygroscopic OC mass in favor of more hygroscopic inorganic salt with increasing particle size. However, the mechanism behind this is not fully understood. We hypothesize that divalent cations such as Ca^{2+} and Mg^{2+}, which are enriched in smaller SSA particles, may engage in cation-mediated coadsorption with OC material, such as deprotonated fatty acids and lipopolysaccharides, with limited interactions with monovalent Na^+ or K^+.[4,5,54] This coadsorption could drive more OC into smaller SSA particles, representing a process similar to forming TEP or hydrogels.[45,97−99] TEP and hydrogels are viscous polymeric materials primarily comprised of organic macromolecules held together by ionic and hydrophobic bonds with dissolved OM.[43] They can assemble in seawater as larger macrogels, reaching sizes of a few meters, or as small as micro- and nanogels, ranging from several micrometers to single nanometers in size, which then transfer into SSA. For instance, Meng and Liu demonstrated enhanced rates of TEP formation in Ca^{2+}-enriched environments compared to Na^+ concentrations in a laboratory study using AFM.[99] Additionally, studies have shown greater enrichment of TEP in increasingly smaller SSA particles.[43,46,47] As Ca^{2+} is more enriched in the smaller SSA particles, electrostatic interactions between Ca^{2+} and the dissolved OM could form these more viscous and bouncier gel particles.

In our model, we simulate the effects of hydrogel formation on SSA viscosity by estimating that for each Ca^{2+} ion, there are two organic anions bound to it (more details of this calculation are in the Supporting Information). Electrostatic interactions between polyanions and divalent cations are thermodynamically favorable during hydrogel formation, with the initial step being the cross-linking of two organic anions with a divalent cation. This initial assembly step of the gel results in a doubling of the molecular weight. This theoretical viscosity adjustment is most significant for the 40 and 60 nm populations, where we estimate, based on a previous study, that 50% and 10%, respectively, of the total inorganic ion mass is Ca^{2+}.[50] For example, in the 40 nm population, while the initial average OC molecular weight was set to 250 g mol^{-1} in the model, the binding of 50% of the inorganic mass fraction to organic molecules increases the average molecular weight to approximately 300 g mol^{-1}. This increase in molecular weight due to complexation with Ca^{2+} in 40 nm nascent SSA significantly raises the estimated viscosity of the OC-rich phase (illustrated in green in Figure 1) and, consequently, the mixed OC/aqueous electrolyte phase (depicted by the blue trace in Figure 1). This enhancement in the viscosity of the mixed SSA particles with decreasing size due to complexation is showcased in the blue shaded region of Figure 1, which shows in the absence of any complexation, 40 nm SSA particles have an estimated $\log_{10}\eta$ of ∼2.5, whereas, with complexation, they have an estimated $\log_{10}\eta$ of ∼4, better reflecting the observed sharp increase in BF with decreasing particle size. As depicted by the black trace in Figure 1, only a minor increase in viscosity, from $\log_{10}\eta \sim 0.6$ to $\log_{10}\eta \sim 0.8$, as the particle size decreases from 60 to 40 nm, can be attributed to the weaker water solubility of $CaCO_3$ compared to NaCl. The

https://doi.org/10.1021/acs.est.4c04312
Environ. Sci. Technol. 2024, 58, 19666−19678

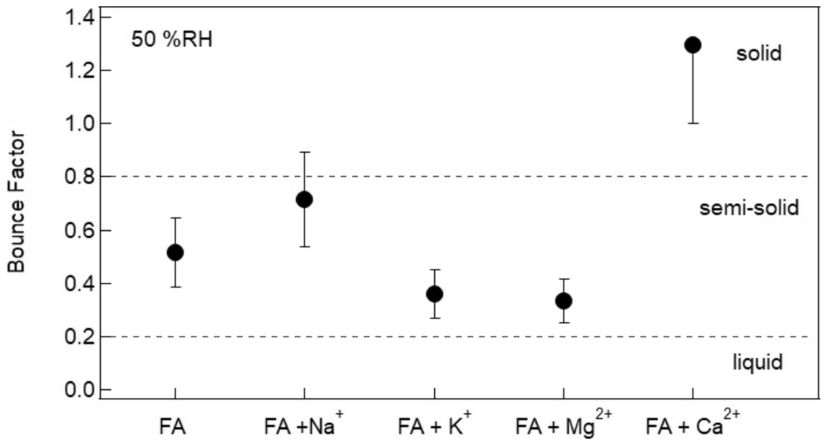

Figure 4. Bounce fractions of atomized aerosol particles comprised of a mixture of fatty acids (FA: lauric acid, myristic acid, palmitic acid, and stearic acid) and individual chloride salts (NaCl, KCl, $MgCl_2$, and $CaCl_2$). The data are the mean of ten replicate measurements for each, and the error bars represent one standard deviation from the mean. The experiments were conducted under nonefflorescing 50% RH. The horizontal dashed lines delineate bounce fractions common to liquid, semisolid, and solid secondary organic aerosol particles.[33]

effects of varying ratios of $CaCO_3$/NaCl on the estimated viscosity are shown in Figure S8.

Additional measurements of the BF of atomized mixtures, consisting of equal ratios of common fatty acids found in SSA (lauric acid, myristic acid, palmitic acid, and stearic acid) with various individual inorganic salts (NaCl, KCl, $MgCl_2$, and $CaCl_2$) are shown in Figure 4. In all cases, except for the aerosol mixtures with $CaCl_2$, the BF indicated semisolid particles at an RH of 50%. In these experiments, the particles did not effloresce. The BF values ranged from 0.3 for the fatty acid mixtures with KCl and $MgCl_2$ to an average of 0.5 to 0.7 for the pure fatty acid mix and fatty acid mixture with NaCl. Notably, the mixture with $CaCl_2$ displayed a BF statistically indistinguishable from 1, suggesting highly viscous or solid-like aerosols.

The higher BF observed in the fatty acid particle mixtures with $CaCl_2$ underscores the potentially significant role of Ca^{2+} in forming more viscous phase states of SSA when mixed with organic molecules as opposed to other cations.[54,97,100] It is worth noting that the pH of the atomizer solution exceeded the pK_a of the various fatty acids, indicating they were in their deprotonated forms upon atomization. Subsequently, the polyanions could then form ionic bonds with the cations responsible for gel formation. While other cations like Na^+, K^+, and Mg^{2+} interact electrostatically with the organic anions in solution, the complexation of Ca^{2+} is expected to be more favorable due to its relatively smaller hydration shell compared to Mg^{2+} and higher valency compared to Na^+ or K^+.[43]

These findings highlight the critical role of gel formation in modulating the size-dependent viscosity of SSA. However, it is essential to consider various factors in the viscosity model, including the organic and inorganic mass fractions, type of aqueous electrolyte, molecular weight, particle density, and hygroscopicity, which are likely to vary with particle size, seawater biological activity, location, and season in the real marine atmospheric environment. Modeling studies on the sensitivities in the estimated SSA viscosity to changing OC molecular weight, κ, Ca^{2+}/Na^+ ratios, and OMF can be found in the Supporting Information (Figures S6−S9). Furthermore, differences in the BF with size could be impacted by differences in the particle's surface tension and the evaporative water losses in the particles from the Kelvin effect (i.e., increasing surface curvature with decreasing particle size) or changes in the RH due to the pressure drops in the impactor. The Supporting Information explores these effects in more detail, and the effects of changing surface tension and particle size of single- and binary-component aerosols representing different nascent SSA constituents are explored in Figure S10.

Moreover, particle morphology should be considered. As illustrated in Figure 1, viscosities can vary widely, ranging from $\log_{10}\eta$ of <1 for the inorganic salt portion to a $\log_{10}\eta$ between ∼2 and ∼4 for the well-mixed OC/aqueous electrolyte particles and even extending to a $\log_{10}\eta > 6$ for the pure OC portion. According to the morphologies and phase states described in Figure 2, the smaller 40 and 60 nm SSA particles, which exhibited more rounded and semisolid phase states, would likely be representative of the modeled well-mixed OC/aqueous electrolyte particles. In contrast, 100 and 200 nm particles, which showed a mixture but a more significant fraction of core−shell than rounded particles, might exhibit different viscosities within the same particle.

3.4. Atmospheric Implications. Understanding how the phase state of SSA changes with size is important for comprehending atmospheric processes, particularly ice and liquid cloud formation. More viscous aerosol particles can serve as better surfaces for heterogeneous freezing and ice nucleation.[36,101−103] This was recently demonstrated by Mehndiratta et al., 2024,[103] showing poorly soluble fatty alcohols, estimated to be semisolids (>10^2 Pa·s) near their onset freezing temperature, freeze heterogeneously at warmer temperatures. On the other hand, larger particles tend to activate into cloud droplets at lower supersaturations and form ice at lower temperatures.[23,96,104]

The smaller, more viscous, nascent SSA particles measured in this study may have extended atmospheric lifetimes with respect to coagulation losses resulting from the reduced coagulation rates of viscous aerosols, though typically, SSA number concentrations in the open ocean are relatively low, so coagulation is less important.[105] However, the viscous medium can extend lifetimes and long-distance transport of toxins and other anthropogenic contaminants from the ocean to locations further inland.[41] Conversely, more efficient nucleation of viscous SSA particles into ice or liquid water cloud droplets could reduce expected atmospheric lifetimes.[106,107] Impor-

https://doi.org/10.1021/acs.est.4c04312
Environ. Sci. Technol. 2024, 58, 19666−19678

tantly, the smaller particles possess larger surface area-to-volume ratios, which could accommodate more adsorbed toxic material on their surfaces.[108] The semisolid nature of the smallest particles observed here may act as a buffer for these contaminants, shielding them from photochemical and oxidative processes that might otherwise remove them from the atmosphere before they are deposited in human lungs.[25,109,110] Furthermore, Kruse et al., 2024[111] showed that the particle's viscosity can affect the molecular detection of aerosol components by extractive electrospray ionization, suggesting that components in smaller SSA may be more difficult to extract than in larger SSA.

In this study, we estimated the viscosity of freshly emitted SSA with respect to size at a constant RH. However, nascent SSA particles may change in physical state and chemical composition over time through aging,[112] potentially modulating viscosity. Further investigations into the viscosity of aged SSA are needed to understand better how their phase states evolve in the atmosphere.

■ ASSOCIATED CONTENT

Data Availability Statement

The data for this publication is available from Open Science Framework at https://osf.io/swdur/.

Supporting Information

The Supporting Information is available free of charge at https://pubs.acs.org/doi/10.1021/acs.est.4c04312.

> Additional experimental and theoretical details for the viscosity and particle effective density calculations, figures of the ambient compared to filtered size distributions, setup, nascent SSA size distributions, viscosity model sensitivities, and differences in BF due to changing surface tension and particle size of single- and binary-component aerosols generated in the lab, and text describing the effects of surface tension, particle surface curvature, and changes in the RH within the impactor on the observed BF (PDF)

■ AUTHOR INFORMATION

Corresponding Author

Jonathan H. Slade − *Department of Chemistry & Biochemistry, University of California San Diego, La Jolla, California 92093, United States;* orcid.org/0000-0002-5026-4229; Email: jhslade@ucsd.edu

Authors

Paul R. Tumminello − *Department of Chemistry & Biochemistry, University of California San Diego, La Jolla, California 92093, United States*

Renee Niles − *Department of Chemistry & Biochemistry, University of California San Diego, La Jolla, California 92093, United States*

Vanessa Valdez − *Department of Chemistry, California State University, Fullerton, California 92831, United States*

Chamika K. Madawala − *Department of Chemistry, University of Iowa, Iowa City, Iowa 52422, United States*

Dilini K. Gamage − *Department of Chemistry, University of Iowa, Iowa City, Iowa 52422, United States*

Ke'La A. Kimble − *Department of Chemistry & Biochemistry, University of California San Diego, La Jolla, California 92093, United States*

Raymond J. Leibensperger, III − *Scripps Institution of Oceanography, University of California San Deigo, San Diego, California 92093, United States*

Chunxu Huang − *Lyles School of Civil Engineering, Purdue University, West Lafayette, Indiana 47907, United States*

Chathuri Kaluarachchi − *Department of Chemistry, University of Iowa, Iowa City, Iowa 52422, United States;* orcid.org/0000-0003-2538-3952

Julie Dinasquet − *Scripps Institution of Oceanography, University of California San Deigo, San Diego, California 92093, United States*

Francesca Malfatti − *Scripps Institution of Oceanography, University of California San Deigo, San Diego, California 92093, United States; Department of Life Sciences, Universita' degli Studi di Trieste, Trieste 34127, Italy*

Christopher Lee − *Scripps Institution of Oceanography, University of California San Deigo, San Diego, California 92093, United States*

Grant B. Deane − *Scripps Institution of Oceanography, University of California San Deigo, San Diego, California 92093, United States*

M. Dale Stokes − *Scripps Institution of Oceanography, University of California San Deigo, San Diego, California 92093, United States*

Elizabeth Stone − *Department of Chemistry, University of Iowa, Iowa City, Iowa 52422, United States;* orcid.org/0000-0003-0078-141X

Alexei Tivanski − *Department of Chemistry, University of Iowa, Iowa City, Iowa 52422, United States;* orcid.org/0000-0002-1528-2421

Kimberly A. Prather − *Department of Chemistry & Biochemistry, University of California San Diego, La Jolla, California 92093, United States; Scripps Institution of Oceanography, University of California San Deigo, San Diego, California 92093, United States*

Brandon E. Boor − *Lyles School of Civil Engineering, Purdue University, West Lafayette, Indiana 47907, United States;* orcid.org/0000-0003-1011-4100

Complete contact information is available at: https://pubs.acs.org/10.1021/acs.est.4c04312

Author Contributions

P.R.T. and J.H.S. conceptualized the study and wrote the paper. P.R.T., R.N., V.V., and C.H. performed the bounce measurements. B.B. and J.H.S. supervised the particle bounce measurements. C.K.M., C.K., and A.T. conducted the AFM analysis. D.K.G. and E.S. measured aerosol organic mass fractions. J.D. and F.M. monitored the seawater biological activity. K.A.K., R.J.L., III. G.B.D., M.D.S., and K.A.P. supervised SOARS. All authors contributed intellectually to the manuscript.

Notes

The authors declare no competing financial interest.

■ ACKNOWLEDGMENTS

This work was funded by the National Science Foundation (NSF) through the NSF Center for Aerosol Impacts on Chemistry of the Environment (CAICE) under Grant CHE-1801971. Thank you to the CHAOS team for their hard work throughout the experimental campaign. We would also like to thank Joseph Mayer, Robert Klidy, and the Scripps Institution of Oceanography Marine Science Development Center team.

The views and opinions expressed in this material solely belong to the authors and do not necessarily represent the opinions, findings, or conclusions of the National Science Foundation.

REFERENCES

(1) Gong, S. L.; Barrie, L. A.; Lazare, M. Canadian Aerosol Module (CAM): A size-segregated simulation of atmospheric aerosol processes for climate and air quality models 2. Global sea-salt aerosol and its budgets. *J. Geophys. Res. Atmos.* **2002**, *107* (D24), 4779.

(2) Prather, K. A.; Bertram, T. H.; Grassian, V. H.; Deane, G. B.; Stokes, M. D.; Demott, P. J.; Aluwihare, L. I.; Palenik, B. P.; Azam, F.; Seinfeld, J. H.; et al. Bringing the ocean into the laboratory to probe the chemical complexity of sea spray aerosol. *Proc. Natl. Acad. Sci. U.S.A.* **2013**, *110* (19), 7550−7555.

(3) Schiffer, J. M.; Mael, L. E.; Prather, K. A.; Amaro, R. E.; Grassian, V. H. Sea spray aerosol: Where marine biology meets atmospheric chemistry. *ACS Cent. Sci.* **2018**, *4* (12), 1617−1623.

(4) Schill, S.; Burrows, S.; Hasenecz, E.; Stone, E.; Bertram, T. The impact of divalent cations on the enrichment of soluble saccharides in primary sea spray aerosol. *Atmosphere* **2018**, *9* (12), 476.

(5) Schill, S. R.; Collins, D. B.; Lee, C.; Morris, H. S.; Novak, G. A.; Prather, K. A.; Quinn, P. K.; Sultana, C. M.; Tivanski, A. V.; Zimmermann, K.; et al. The impact of aerosol particle mixing state on the hygroscopicity of sea spray aerosol. *ACS Cent. Sci.* **2015**, *1* (3), 132−141.

(6) Bertram, T. H.; Cochran, R. E.; Grassian, V. H.; Stone, E. A. Sea spray aerosol chemical composition: elemental and molecular mimics for laboratory studies of heterogeneous and multiphase reactions. *Chem. Soc. Rev.* **2018**, *47* (7), 2374−2400.

(7) Cochran, R. E.; Laskina, O.; Trueblood, J. V.; Estillore, A. D.; Morris, H. S.; Jayarathne, T.; Sultana, C. M.; Lee, C.; Lin, P.; Laskin, J.; et al. Molecular diversity of sea spray aerosol particles: impact of ocean biology on particle composition and hygroscopicity. *Chem* **2017**, *2* (5), 655−667.

(8) Collins, D. B.; Ault, A. P.; Moffet, R. C.; Ruppel, M. J.; Cuadra-Rodriguez, L. A.; Guasco, T. L.; Corrigan, C. E.; Pedler, B. E.; Azam, F.; Aluwihare, L. I.; et al. Impact of marine biogeochemistry on the chemical mixing state and cloud forming ability of nascent sea spray aerosol. *J. Geophys. Res. Atmos.* **2013**, *118* (15), 8553−8565.

(9) Collins, D. B.; Zhao, D. F.; Ruppel, M. J.; Laskina, O.; Grandquist, J. R.; Modini, R. L.; Stokes, M. D.; Russell, L. M.; Bertram, T. H.; Grassian, V. H.; et al. Direct aerosol chemical composition measurements to evaluate the physicochemical differences between controlled sea spray aerosol generation schemes. *Atmos. Meas. Technol.* **2014**, *7* (11), 3667−3683.

(10) Jayarathne, T.; Sultana, C. M.; Lee, C.; Malfatti, F.; Cox, J. L.; Pendergraft, M. A.; Moore, K. A.; Azam, F.; Tivanski, A. V.; Cappa, C. D.; et al. Enrichment of saccharides and divalent cations in sea spray aerosol during two phytoplankton blooms. *Environ. Sci. Technol.* **2016**, *50* (21), 11511−11520.

(11) Lee, H. D.; Morris, H. S.; Laskina, O.; Sultana, C. M.; Lee, C.; Jayarathne, T.; Cox, J. L.; Wang, X.; Hasenecz, E. S.; DeMott, P. J.; et al. Organic enrichment, physical phase state, and surface tension depression of nascent core−shell sea spray aerosols during two phytoplankton blooms. *ACS Earth Space Chem.* **2020**, *4* (4), 650−660.

(12) Angle, K. J.; Crocker, D. R.; Simpson, R. M. C.; Mayer, K. J.; Garofalo, L. A.; Moore, A. N.; Mora Garcia, S. L.; Or, V. W.; Srinivasan, S.; Farhan, M.; et al. Acidity across the interface from the ocean surface to sea spray aerosol. *Proc. Natl. Acad. Sci. U.S.A.* **2021**, *118* (2), 1−6.

(13) de Leeuw, G.; Andreas, E. L.; Anguelova, M. D.; Fairall, C. W.; Lewis, E. R.; O'Dowd, C.; Schulz, M.; Schwartz, S. E. Production flux of sea spray aerosol. *Rev. Geophys.* **2011**, *49* (2), RG2001.

(14) Wilson, T. W.; Ladino, L. A.; Alpert, P. A.; Breckels, M. N.; Brooks, I. M.; Browse, J.; Burrows, S. M.; Carslaw, K. S.; Huffman, J. A.; Judd, C.; et al. A marine biogenic source of atmospheric ice-nucleating particles. *Nature* **2015**, *525* (7568), 234−238.

(15) DeMott, P. J.; Hill, T. C.; McCluskey, C. S.; Prather, K. A.; Collins, D. B.; Sullivan, R. C.; Ruppel, M. J.; Mason, R. H.; Irish, V. E.; Lee, T.; et al. Sea spray aerosol as a unique source of ice nucleating particles. *Proc. Natl. Acad. Sci. U.S.A.* **2016**, *113* (21), 5797−5803.

(16) George, I. J.; Abbatt, J. P. Heterogeneous oxidation of atmospheric aerosol particles by gas-phase radicals. *Nat. Chem.* **2010**, *2* (9), 713−722.

(17) Zelenyuk, A.; Imre, D.; Cuadra-Rodriguez, L. A.; Ellison, B. Measurements and interpretation of the effect of a soluble organic surfactant on the density, shape and water uptake of hygroscopic particles. *J. Aerosol Sci.* **2007**, *38* (9), 903−923.

(18) Bzdek, B. R.; Reid, J. P.; Malila, J.; Prisle, N. L. The surface tension of surfactant-containing, finite volume droplets. *Proc. Natl. Acad. Sci. U.S.A.* **2020**, *117* (15), 8335−8343.

(19) Cravigan, L. T.; Mallet, M. D.; Vaattovaara, P.; Harvey, M. J.; Law, C. S.; Modini, R. L.; Russell, L. M.; Stelcer, E.; Cohen, D. D.; Olsen, G.; et al. Sea spray aerosol organic enrichment, water uptake and surface tension effects. *Atmos. Chem. Phys.* **2020**, *20* (13), 7955−7977.

(20) Davies, J. F.; Zuend, A.; Wilson, K. R. Technical note: The role of evolving surface tension in the formation of cloud droplets. *Atmos. Chem. Phys.* **2019**, *19* (5), 2933−2946.

(21) Koop, T.; Bookhold, J.; Shiraiwa, M.; Poschl, U. Glass transition and phase state of organic compounds: dependency on molecular properties and implications for secondary organic aerosols in the atmosphere. *Phys. Chem. Chem. Phys.* **2011**, *13* (43), 19238−19255.

(22) Lu, J. W.; Rickards, A. M.; Walker, J. S.; Knox, K. J.; Miles, R. E.; Reid, J. P.; Signorell, R. Timescales of water transport in viscous aerosol: measurements on sub-micron particles and dependence on conditioning history. *Phys. Chem. Chem. Phys.* **2014**, *16* (21), 9819−9830.

(23) Petters, M.; Kasparoglu, S. Predicting the influence of particle size on the glass transition temperature and viscosity of secondary organic material. *Sci. Rep.* **2020**, *10* (1), 15170.

(24) Reid, J. P.; Bertram, A. K.; Topping, D. O.; Laskin, A.; Martin, S. T.; Petters, M. D.; Pope, F. D.; Rovelli, G. The viscosity of atmospherically relevant organic particles. *Nat. Commun.* **2018**, *9* (1), 956.

(25) Shiraiwa, M.; Ammann, M.; Koop, T.; Poschl, U. Gas uptake and chemical aging of semisolid organic aerosol particles. *Proc. Natl. Acad. Sci. U.S.A.* **2011**, *108* (27), 11003−11008.

(26) Shiraiwa, M.; Li, Y.; Tsimpidi, A. P.; Karydis, V. A.; Berkemeier, T.; Pandis, S. N.; Lelieveld, J.; Koop, T.; Poschl, U. Global distribution of particle phase state in atmospheric secondary organic aerosols. *Nat. Commun.* **2017**, *8*, 15002.

(27) Shiraiwa, M.; Zuend, A.; Bertram, A. K.; Seinfeld, J. H. Gas-particle partitioning of atmospheric aerosols: interplay of physical state, non-ideal mixing and morphology. *Phys. Chem. Chem. Phys.* **2013**, *15* (27), 11441−11453.

(28) Dette, H. P.; Koop, T. Glass formation processes in mixed inorganic/organic aerosol particles. *J. Phys. Chem. A* **2015**, *119* (19), 4552−4561.

(29) Li, Y.; Day, D. A.; Stark, H.; Jimenez, J. L.; Shiraiwa, M. Predictions of the glass transition temperature and viscosity of organic aerosols from volatility distributions. *Atmos. Chem. Phys.* **2020**, *20* (13), 8103−8122.

(30) Virtanen, A.; Joutsensaari, J.; Koop, T.; Kannosto, J.; Yli-Pirila, P.; Leskinen, J.; Makela, J. M.; Holopainen, J. K.; Poschl, U.; Kulmala, M.; et al. An amorphous solid state of biogenic secondary organic aerosol particles. *Nature* **2010**, *467* (7317), 824−827.

(31) Liu, Y.; Wu, Z.; Huang, X.; Shen, H.; Bai, Y.; Qiao, K.; Meng, X.; Hu, W.; Tang, M.; He, L. Aerosol phase state and its link to chemical composition and liquid water content in a subtropical coastal megacity. *Environ. Sci. Technol.* **2019**, *53* (9), 5027−5033.

(32) Marshall, F. H.; Miles, R. E. H.; Song, Y. C.; Ohm, P. B.; Power, R. M.; Reid, J. P.; Dutcher, C. S. Diffusion and reactivity in ultraviscous aerosol and the correlation with particle viscosity. *Chem. Sci.* **2016**, *7* (2), 1298−1308.

https://doi.org/10.1021/acs.est.4c04312
Environ. Sci. Technol. 2024, 58, 19666−19678

(33) Pajunoja, A.; Hu, W.; Leong, Y. J.; Taylor, N. F.; Miettinen, P.; Palm, B. B.; Mikkonen, S.; Collins, D. R.; Jimenez, J. L.; Virtanen, A. Phase state of ambient aerosol linked with water uptake and chemical aging in the southeastern US. *Atmos. Chem. Phys.* **2016**, *16* (17), 11163−11176.
(34) DeRieux, W.-S. W.; Li, Y.; Lin, P.; Laskin, J.; Laskin, A.; Bertram, A. K.; Nizkorodov, S. A.; Shiraiwa, M. Predicting the glass transition temperature and viscosity of secondary organic material using molecular composition. *Atmos. Chem. Phys.* **2018**, *18* (9), 6331−6351.
(35) Gervasi, N. R.; Topping, D. O.; Zuend, A. A predictive group-contribution model for the viscosity of aqueous organic aerosol. *Atmos. Chem. Phys.* **2020**, *20* (5), 2987−3008.
(36) Berkemeier, T.; Shiraiwa, M.; Pöschl, U.; Koop, T. Competition between water uptake and ice nucleation by glassy organic aerosol particles. *Atmos. Chem. Phys.* **2014**, *14* (22), 12513−12531.
(37) Knopf, D. A.; Alpert, P. A.; Wang, B. The role of organic aerosol in atmospheric ice nucleation: A review. *ACS Earth Space Chem.* **2018**, *2* (3), 168−202.
(38) King, S. M.; Butcher, A. C.; Rosenoern, T.; Coz, E.; Lieke, K. I.; de Leeuw, G.; Nilsson, E. D.; Bilde, M. Investigating primary marine aerosol properties: CCN activity of sea salt and mixed inorganic-organic particles. *Environ. Sci. Technol.* **2012**, *46* (19), 10405−10412.
(39) Ault, A. P.; Moffet, R. C.; Baltrusaitis, J.; Collins, D. B.; Ruppel, M. J.; Cuadra-Rodriguez, L. A.; Zhao, D.; Guasco, T. L.; Ebben, C. J.; Geiger, F. M.; et al. Size-dependent changes in sea spray aerosol composition and properties with different seawater conditions. *Environ. Sci. Technol.* **2013**, *47* (11), 5603−5612.
(40) Freedman, M. A. Phase separation in organic aerosol. *Chem. Soc. Rev.* **2017**, *46* (24), 7694−7705.
(41) Zelenyuk, A.; Imre, D. G.; Wilson, J.; Bell, D. M.; Suski, K. J.; Shrivastava, M.; Beranek, J.; Alexander, M. L.; Kramer, A. L.; Massey Simonich, S. L. The effect of gas-phase polycyclic aromatic hydrocarbons on the formation and properties of biogenic secondary organic aerosol particles. *Faraday Discuss.* **2017**, *200*, 143−164.
(42) Tumminello, P. R.; James, R. C.; Kruse, S.; Kawasaki, A.; Cooper, A.; Guadalupe-Diaz, I.; Zepeda, K. L.; Crocker, D. R.; Mayer, K. J.; Sauer, J. S.; et al. Evolution of sea spray aerosol particle phase state across a phytoplankton bloom. *ACS Earth Space Chem.* **2021**, *5* (11), 2995−3007.
(43) Verdugo, P. Marine microgels. *Annu. Rev. Mar. Sci.* **2012**, *4*, 375−400.
(44) Engel, A.; Endres, S.; Galgani, L.; Schartau, M. Marvelous marine microgels: on the distribution and impact of gel-like particles in the oceanic water-column. *Front. Mar. Sci.* **2020**, *7*, 405.
(45) Passow, U. Transparent exopolymer particles (TEP) in aquatic environments. *Prog. Oceanogr.* **2002**, *55*, 287−333.
(46) van Pinxteren, M.; Robinson, T.-B.; Zeppenfeld, S.; Gong, X.; Bahlmann, E.; Fomba, K. W.; Triesch, N.; Stratmann, F.; Wurl, O.; Engel, A.; et al. High number concentrations of transparent exopolymer particles in ambient aerosol particles and cloud water − a case study at the tropical Atlantic Ocean. *Atmos. Chem. Phys.* **2022**, *22* (8), 5725−5742.
(47) Aller, J. Y.; Radway, J. C.; Kilthau, W. P.; Bothe, D. W.; Wilson, T. W.; Vaillancourt, R. D.; Quinn, P. K.; Coffman, D. J.; Murray, B. J.; Knopf, D. A. Size-resolved characterization of the polysaccharidic and proteinaceous components of sea spray aerosol. *Atmos. Environ.* **2017**, *154*, 331−347.
(48) Facchini, M. C.; Rinaldi, M.; Decesari, S.; Carbone, C.; Finessi, E.; Mircea, M.; Fuzzi, S.; Ceburnis, D.; Flanagan, R.; Nilsson, E. D.; et al. Primary submicron marine aerosol dominated by insoluble organic colloids and aggregates. *Geophys. Res. Lett.* **2008**, *35* (17), L17814.
(49) Orellana, M. V.; Matrai, P. A.; Leck, C.; Rauschenberg, C. D.; Lee, A. M.; Coz, E. Marine microgels as a source of cloud condensation nuclei in the high Arctic. *Proc. Natl. Acad. Sci. U.S.A.* **2011**, *108* (33), 13612−13617.
(50) Salter, M. E.; Hamacher-Barth, E.; Leck, C.; Werner, J.; Johnson, C. M.; Riipinen, I.; Nilsson, E. D.; Zieger, P. Calcium enrichment in sea spray aerosol particles. *Geophys. Res. Lett.* **2016**, *43* (15), 8277−8285.
(51) Brooks, S. D.; Thornton, D. C. O. Marine aerosols and clouds. *Annu. Rev. Mar. Sci.* **2018**, *10*, 289−313.
(52) Nguyen, Q. T.; Kjær, K. H.; Kling, K. I.; Boesen, T.; Bilde, M. Impact of fatty acid coating on the CCN activity of sea salt particles. *Tellus B* **2017**, *69* (1), 1304064.
(53) Miñambres, L.; Méndez, E.; Sánchez, M. N.; Castaño, F.; Basterretxea, F. J. The effect of low solubility organic acids on the hygroscopicity of sodium halide aerosols. *Atmos. Chem. Phys.* **2014**, *14* (20), 11409−11425.
(54) Lee, C.; Dommer, A. C.; Schiffer, J. M.; Amaro, R. E.; Grassian, V. H.; Prather, K. A. Cation-driven lipopolysaccharide morphological changes impact heterogeneous reactions of nitric acid with sea spray aerosol particles. *J. Phys. Chem. Lett.* **2021**, *12* (20), 5023−5029.
(55) Lee, H. D.; Wigley, S.; Lee, C.; Or, V. W.; Hasenecz, E. S.; Stone, E. A.; Grassian, V. H.; Prather, K. A.; Tivanski, A. V. Physicochemical mixing state of sea spray aerosols: morphologies exhibit size dependence. *ACS Earth Space Chem.* **2020**, *4* (9), 1604−1611.
(56) Kaluarachchi, C. P.; Or, V. W.; Lan, Y.; Madawala, C. K.; Hasenecz, E. S.; Crocker, D. R.; Morris, C. K.; Lee, H. D.; Mayer, K. J.; Sauer, J. S.; et al. Size-dependent morphology, composition, phase state, and water uptake of nascent submicrometer sea spray aerosols during a phytoplankton bloom. *ACS Earth Space Chem.* **2022**, *6* (1), 116−130.
(57) Bulatovic, I.; Igel, A. L.; Leck, C.; Heintzenberg, J.; Riipinen, I.; Ekman, A. M. L. The importance of Aitken mode aerosol particles for cloud sustenance in the summertime high Arctic − a simulation study supported by observational data. *Atmos. Chem. Phys.* **2021**, *21* (5), 3871−3897.
(58) Sauer, J. S.; Mayer, K. J.; Lee, C.; Alves, M. R.; Amiri, S.; Bahaveolos, C. J.; Franklin, E. B.; Crocker, D. R.; Dang, D.; Dinasquet, J.; et al. The Sea Spray Chemistry and Particle Evolution study (SeaSCAPE): overview and experimental methods. *Environ. Sci. Process. Impacts* **2022**, *24* (2), 290−315.
(59) Kannosto, J.; Yli-Pirila, P.; Hao, L.-Q.; Leskinen, J.; Jokiniemi, J.; Makela, J. M.; Joutsensaari, J.; Laaksonen, A.; Worsnop, D. R.; Keskinen, J.; et al. Bounce characteristics of α-pinene-derived SOA particles with implications to physical phase. *Boreal Environ. Res.* **2013**, *18*, 329−340.
(60) Slade, J. H.; Ault, A. P.; Bui, A. T.; Ditto, J. C.; Lei, Z.; Bondy, A. L.; Olson, N. E.; Cook, R. D.; Desrochers, S. J.; Harvey, R. M.; et al. Bouncier particles at night: Biogenic secondary organic aerosol chemistry and sulfate drive diel variations in the aerosol phase in a mixed forest. *Environ. Sci. Technol.* **2019**, *53* (9), 4977−4987.
(61) Saukko, E.; Kuuluvainen, H.; Virtanen, A. A method to resolve the phase state of aerosol particles. *Atmos. Meas. Technol.* **2012**, *5* (1), 259−265.
(62) Jain, S.; Petrucci, G. A. A new method to measure aerosol particle bounce using a cascade electrical low pressure impactor. *Aerosol Sci. Technol.* **2015**, *49* (6), 390−399.
(63) Mayer, K. J.; Sauer, J. S.; Dinasquet, J.; Prather, K. A. CAICE studies: Insights from a decade of ocean-atmosphere experiments in the laboratory. *Acc. Chem. Res.* **2020**, *53* (11), 2510−2520.
(64) Madawala, C. K.; Molina, C.; Kim, D.; Gamage, D. K.; Sun, M. N.; Leibensperger, R. J., III; Mehndiratta, L.; Lee, J.; Kaluarachchi, C. P.; Kimble, K. A.; et al. Effects of wind speed on size-dependent morphology and composition of sea spray aerosols. *ACS Earth Space Chem.* **2024**, *8*, 1609−1622.
(65) Hsu, S. A.; Meindl, E. A.; Gilhousen, D. B. Determining the power-law wind-profile exponent under near-neutral stability conditions at sea. *J. Appl. Meteorol. Clim.* **1994**, *33* (6), 757−765.
(66) Monahan, E. C.; O'Muircheartaigh, I. G. Whitecaps and the passive remote sensing of the ocean surface. *Int. J. Remote Sens.* **1986**, *7* (5), 627−642.

https://doi.org/10.1021/acs.est.4c04312
Environ. Sci. Technol. 2024, 58, 19666−19678

(67) Schwier, A. N.; Rose, C.; Asmi, E.; Ebling, A. M.; Landing, W. M.; Marro, S.; Pedrotti, M. L.; Sallon, A.; Iuculano, F.; Agusti, S.; et al. Primary marine aerosol emissions from the Mediterranean Sea during pre-bloom and oligotrophic conditions: correlations to seawater chlorophyll-a from a mesocosm study. *Atmos. Chem. Phys.* **2015**, *15* (14), 7961−7976.
(68) Ovadnevaite, J.; Manders, A.; de Leeuw, G.; Ceburnis, D.; Monahan, C.; Partanen, A. I.; Korhonen, H.; O'Dowd, C. D. A sea spray aerosol flux parameterization encapsulating wave state. *Atmos. Chem. Phys.* **2014**, *14* (4), 1837−1852.
(69) Bau, S.; Bémer, D.; Grippari, F.; Appert-Collin, J.-C.; Thomas, D. Determining the effective density of airborne nanoparticles using multiple charging correction in a tandem DMA/ELPI setup. *J. Nanopart. Res.* **2014**, *16* (10), 2629.
(70) Fischer, K. B.; Petrucci, G. A. Utilizing an electrical low-pressure impactor to indirectly probe water uptake via particle bounce measurements. *Atmos. Meas. Technol.* **2021**, *14* (12), 7565−7577.
(71) Jiang, J.; Ding, X.; Isaacson, K. P.; Tasoglou, A.; Huber, H.; Shah, A. D.; Jung, N.; Boor, B. E. Ethanol-based disinfectant sprays drive rapid changes in the chemical composition of indoor air in residential buildings. *J. Hazard. Mater. Lett.* **2021**, *2*, 100042.
(72) Jiang, J.; Ding, X.; Tasoglou, A.; Huber, H.; Shah, A. D.; Jung, N.; Boor, B. E. Real-time measurements of botanical disinfectant emissions, transformations, and multiphase inhalation exposures in buildings. *Environ. Sci. Technol. Lett.* **2021**, *8* (7), 558−566.
(73) Wu, T.; Boor, B. E. Characterization of a thermal aerosol generator for HVAC filtration experiments (RP-1734). *Sci. Technol. Built Environ.* **2020**, *26* (6), 816−834.
(74) Estillore, A. D.; Morris, H. S.; Or, V. W.; Lee, H. D.; Alves, M. R.; Marciano, M. A.; Laskina, O.; Qin, Z.; Tivanski, A. V.; Grassian, V. H. Linking hygroscopicity and the surface microstructure of model inorganic salts, simple and complex carbohydrates, and authentic sea spray aerosol particles. *Phys. Chem. Chem. Phys.* **2017**, *19* (31), 21101−21111.
(75) Lee, H. D.; Kaluarachchi, C. P.; Hasenecz, E. S.; Zhu, J. Z.; Popa, E.; Stone, E. A.; Tivanski, A. V. Effect of dry or wet substrate deposition on the organic volume fraction of core−shell aerosol particles. *Atmos. Meas. Technol.* **2019**, *12* (3), 2033−2042.
(76) Madawala, C. K.; Lee, H. D.; Kaluarachchi, C. P.; Tivanski, A. V. Probing the water uptake and phase state of individual sucrose nanoparticles using atomic force microscopy. *ACS Earth Space Chem.* **2021**, *5* (10), 2612−2620.
(77) Madawala, C. K.; Lee, H. D.; Kaluarachchi, C. P.; Tivanski, A. V. Quantifying the viscosity of individual submicrometer semisolid particles using atomic force microscopy. *Anal. Chem.* **2023**, *95* (39), 14566−14572.
(78) Ray, K. K.; Lee, H. D.; Gutierrez, M. A.; Chang, F. J.; Tivanski, A. V. Correlating 3D morphology, phase state, and viscoelastic properties of individual substrate-deposited particles. *Anal. Chem.* **2019**, *91* (12), 7621−7630.
(79) Lee, H. D.; Ray, K. K.; Tivanski, A. V. Solid, semisolid, and liquid phase states of individual submicrometer particles directly probed using atomic force microscopy. *Anal. Chem.* **2017**, *89* (23), 12720−12726.
(80) Cappa, C. D.; Ristenpart, W. D.; Barreda, S.; Bouvier, N. M.; Levintal, E.; Wexler, A. S.; Roman, S. A. A highly efficient cloth facemask design. *Aerosol Sci. Technol.* **2022**, *56* (1), 12−28.
(81) Birch, M. E.; Cary, R. A. Elemental carbon-based method for monitoring occupational exposures to particulate diesel exhaust. *Aerosol Sci. Technol.* **1996**, *25* (3), 221−241.
(82) Shafer, M. M.; Perkins, D. A.; Antkiewicz, D. S.; Stone, E. A.; Quraishi, T. A.; Schauer, A. A. Reactive oxygen species activity and chemical speciation of size-fractionated atmospheric particulate matter from Lahore, Pakistan: An important role for transition metals. *J. Environ. Monitor* **2010**, *12*, 704−715.
(83) Holland, H. D. *The Chemistry of the Atmosphere and Oceans*; John Wiley & Sons Inc, 1978.
(84) Saukko, E.; Lambe, A. T.; Massoli, P.; Koop, T.; Wright, J. P.; Croasdale, D. R.; Pedernera, D. A.; Onasch, T. B.; Laaksonen, A.; Davidovits, P.; et al. Humidity-dependent phase state of SOA particles from biogenic and anthropogenic precursors. *Atmos. Chem. Phys.* **2012**, *12* (16), 7517−7529.
(85) Wang, X.; Sultana, C. M.; Trueblood, J.; Hill, T. C.; Malfatti, F.; Lee, C.; Laskina, O.; Moore, K. A.; Beall, C. M.; McCluskey, C. S.; et al. Microbial control of sea spray aerosol composition: A tale of two blooms. *ACS Cent. Sci.* **2015**, *1* (3), 124−131.
(86) Martin, S. T. Phase Transitions of Aqueous Atmospheric Particles. *Chem. Rev.* **2000**, *100* (9), 3403−3454.
(87) Bateman, A. P.; Bertram, A. K.; Martin, S. T. Hygroscopic influence on the semisolid-to-liquid transition of secondary organic materials. *J. Phys. Chem. A* **2015**, *119* (19), 4386−4395.
(88) Bateman, A. P.; Belassein, H.; Martin, S. T. Impactor apparatus for the study of particle rebound: relative humidity and capillary forces. *Aerosol Sci. Technol.* **2014**, *48* (1), 42−52.
(89) Winkler, P. Relative humidity and the adhesion of atmospheric particles to the plates of impactors. *Aerosol Sci.* **1974**, *5*, 235−240.
(90) Rostedt, A.; Marjamäki, M.; Keskinen, J. Modification of the ELPI to measure mean particle effective density in real-time. *J. Aerosol Sci.* **2009**, *40* (9), 823−831.
(91) Rissler, J.; Nordin, E. Z.; Eriksson, A. C.; Nilsson, P. T.; Frosch, M.; Sporre, M. K.; Wierzbicka, A.; Svenningsson, B.; Londahl, J.; Messing, M. E.; et al. Effective density and mixing state of aerosol particles in a near-traffic urban environment. *Environ. Sci. Technol.* **2014**, *48* (11), 6300−6308.
(92) Nakao, S.; Tang, P.; Tang, X.; Clark, C. H.; Qi, L.; Seo, E.; Asa-Awuku, A.; Cocker, D. Density and elemental ratios of secondary organic aerosol: Application of a density prediction method. *Atmos. Environ.* **2013**, *68*, 273−277.
(93) Gantt, B.; Meskhidze, N.; Facchini, M. C.; Rinaldi, M.; Ceburnis, D.; O'Dowd, C. D. Wind speed dependent size-resolved parameterization for the organic mass fraction of sea spray aerosol. *Atmos. Chem. Phys.* **2011**, *11* (16), 8777−8790.
(94) Rinaldi, M.; Fuzzi, S.; Decesari, S.; Marullo, S.; Santoleri, R.; Provenzale, A.; von Hardenberg, J.; Ceburnis, D.; Vaishya, A.; O'Dowd, C. D.; et al. Is chlorophyll-a the best surrogate for organic matter enrichment in submicron primary marine aerosol? *J. Geophys. Res. Atmos.* **2013**, *118* (10), 4964−4973.
(95) Power, R. M.; Simpson, S. H.; Reid, J. P.; Hudson, A. J. The transition from liquid to solid-like behaviour in ultrahigh viscosity aerosol particles. *Chem. Sci.* **2013**, *4* (6), 2597−2604.
(96) Petters, M.; Kreidenweis, S. M. A single parameter representation of hygroscopic growth and cloud condensation nucleus activity. *Atmos. Chem. Phys.* **2007**, *7* (8), 1961−1971.
(97) Su, B.; Bi, X.; Zhang, Z.; Liang, Y.; Song, C.; Wang, T.; Hu, Y.; Li, L.; Zhou, Z.; Yan, J.; et al. Enrichment of calcium in sea spray aerosol: insights from bulk measurements and individual particle analysis during the R/V Xuelong cruise in the summertime in Ross Sea, Antarctica. *Atmos. Chem. Phys.* **2023**, *23* (18), 10697−10711.
(98) Li, S.; Winters, H.; Jeong, S.; Emwas, A.-H.; Vigneswaran, S.; Amy, G. L. Marine bacterial transparent exopolymer particles (TEP) and TEP precursors: Characterization and RO fouling potential. *Desalination* **2016**, *379*, 68−74.
(99) Meng, S.; Liu, Y. New insights into transparent exopolymer particles (TEP) formation from precursor materials at various Na +/Ca2+ ratios. *Sci. Rep.* **2016**, *6*, 19747.
(100) Hasenecz, E. S.; Kaluarachchi, C. P.; Lee, H. D.; Tivanski, A. V.; Stone, E. A. Saccharide transfer to sea spray aerosol enhanced by surface activity, calcium, and protein interactions. *ACS Earth Space Chem.* **2019**, *3* (11), 2539−2548.
(101) Wilson, T. W.; Murray, B. J.; Wagner, R.; Möhler, O.; Saathoff, H.; Schnaiter, M.; Skrotzki, J.; Price, H. C.; Malkin, T. L.; Dobbie, S.; et al. Glassy aerosols with a range of compositions nucleate ice heterogeneously at cirrus temperatures. *Atmos. Chem. Phys.* **2012**, *12* (18), 8611−8632.
(102) Murray, B. J.; Wilson, T. W.; Dobbie, S.; Cui, Z.; Al-Jumur, S. M. R. K.; Möhler, O.; Schnaiter, M.; Wagner, R.; Benz, S.; Niemand, M.; et al. Heterogeneous nucleation of ice particles on glassy aerosols under cirrus conditions. *Nat. Geosci.* **2010**, *3* (4), 233−237.

(103) Mehndiratta, L.; Lyp, A.; Slade, J.; Grassian, V. Immersion Ice Nucleation of Atmospherically Relevant Lipid Particles. *Environ. Sci.: Atmos.* **2024**.
(104) Petters, M.; Kreidenweis, S. M. A single parameter representation of hygroscopic growth and cloud condensation nucleus activity − Part 2: Including solubility. *Atmos. Chem. Phys.* **2008**, *8* (20), 6273−6279.
(105) Alam, M. K. The Effect of van der Waals and Viscous Forces on Aerosol Coagulation. *Aerosol Sci. Technol.* **1987**, *6*, 41−52.
(106) Schill, G. P.; Tolbert, M. A. Heterogeneous ice nucleation on simulated sea-spray aerosol using Raman microscopy. *J. Phys. Chem. C* **2014**, *118* (50), 29234−29241.
(107) Schill, G. P.; Tolbert, M. A. Heterogeneous ice nucleation on phase-separated organic-sulfate particles: effect of liquid vs. glassy coatings. *Atmos. Chem. Phys.* **2013**, *13* (9), 4681−4695.
(108) Kwon, H. S.; Ryu, M. H.; Carlsten, C. Ultrafine particles: unique physicochemical properties relevant to health and disease. *Exp. Mol. Med.* **2020**, *52* (3), 318−328.
(109) Kruse, S. M.; Slade, J. H. Heterogeneous and photosensitized oxidative degradation kinetics of the plastic additive bisphenol-A in sea spray aerosol mimics. *J. Phys. Chem. A* **2023**, *127* (21), 4724−4733.
(110) Slade, J. H.; Thalman, R.; Wang, J.; Knopf, D. A. Chemical aging of single and multicomponent biomass burning aerosol surrogate particles by OH: implications for cloud condensation nucleus activity. *Atmos. Chem. Phys.* **2015**, *15* (17), 10183−10201.
(111) Kruse, S. M.; Tumminello, P. R.; Moore, A. N.; Lee, C. S. P.; Prather, K. A.; Slade, J. H. Effects of relative humidity and phase on the molecular detection of nascent sea spray aerosol using extractive electrospray ionization. *Anal. Chem.* **2024**, *96* (31), 12901−12907.
(112) Kaluarachchi, C. P.; Or, V. W.; Lan, Y. L.; Hasenecz, E. S.; Kim, D.; Madawala, C. K.; Dorcé, G. P.; Mayer, K. J.; Sauer, J. S.; Lee, C. S. P.; et al. Effects of atmospheric aging processes on nascent sea spray aerosol physicochemical properties. *ACS Earth Space Chem.* **2022**, *6* (11), 2732−2744.

https://doi.org/10.1021/acs.est.4c04312
Environ. Sci. Technol. 2024, 58, 19666−19678